AGU PUBLICATIONS

Geochemistry, Geophysics, Geosystems

RESEARCH ARTICLE
10.1002/2014GC005369

Key Points:
- Fault parameters are determined for four normal earthquakes in PXR
- The solutions reinforce moderate dip angles for normal faulting events
- The 1996/1998 events are consistent with static stress transfer promoting failure

Supporting Information:
- Readme
- Figures S1–S10

Correspondence to:
H. Wang,
ehwang@163.com

Citation:
Wang, H., J. R. Elliott, T. J. Craig, T. J. Wright, J. Liu-Zeng, and A. Hooper (2014), Normal faulting sequence in the Pumqu-Xainza Rift constrained by InSAR and teleseismic body-wave seismology, *Geochem. Geophys. Geosyst.*, *15*, 2947–2963, doi:10.1002/2014GC005369.

Received 4 APR 2014
Accepted 30 JUN 2014
Accepted article online 4 JUL 2014
Published online 24 JUL 2014

Normal faulting sequence in the Pumqu-Xainza Rift constrained by InSAR and teleseismic body-wave seismology

Hua Wang[1,2], John R. Elliott[3], Timothy J. Craig[4], Tim J. Wright[5], Jing Liu-Zeng[2], and Andrew Hooper[5]

[1]Department of Surveying Engineering, Guangdong University of Technology, Guangzhou, China, [2]State Key Laboratory of Earthquake Dynamics, Institute of Geology, China Earthquake Administration, Beijing, China, [3]COMET, Department of Earth Sciences, University of Oxford, Oxford, UK, [4]Laboratoire de Géologie, Ecole Normale Supérieure, Paris, France, [5]COMET, School of Earth and Environment, University of Leeds, Leeds, UK

Abstract Normal faulting earthquakes play an important role in the deformation of continents, and pose significant seismic hazard, yet important questions remain about their mechanics. We use InSAR and body-wave seismology to compute dislocation models and centroid moment solutions for four normal-faulting earthquakes (M_w 5.7–6.2) that occurred in the Pumqu-Xainza Rift (PXR), southern Tibet, a region where low-angle normal faulting has previously been inferred. We also use the fault locations and slip to investigate the correlation between earthquakes and surface topography, and to calculate stress interactions between the earthquakes. The InSAR and body-wave models give consistent focal mechanisms except for the magnitude of the 1996 event, which may be overestimated due to postseismic deformation in the long-interval interferograms. We calculate the static stress changes due to coseismic slip and find that the 1993 event was too distant to cause triggering of the later events, but that the 1998 event pair occurred in regions of increased Coulomb stress resulting from the 1996 event. All the fault planes found here dip at 40–60°, reinforcing the absence in observations for low-angle normal faulting earthquakes (dip $< 30°$) whose focal planes can be determined unambiguously. The fault planes of the 1993 and 1996 events are not associated with any obvious surface geomorphology, suggesting that sometimes it is unreliable to resolve the focal plane ambiguity by geomorphology, even for M_w 6.2 events. Furthermore, these events occurred outside the center of the rift, indicating that the active faulting is more distributed and over a length-scale at least 25–50 km east-west in extent, rather than confined to the 20 km width seen in the current mapped faulting and topography. These results suggest that seismic hazard in other extensional zones worldwide might also be more broadly distributed than suggested by geomorphology.

1. Introduction

Extensional faulting plays an important role in the deformation of continents, and is prominent in regions such as the Basin and Range province of Western US, the Aegean, the Apennines, and southern Tibet [*Eaton*, 1982; *Wernicke et al*., 1988; *Anderson and Jackson*, 1987; *Taymaz et al*., 1991; *Jackson*, 1994; *Çemen*, 2010; *Molnar and Tapponnier*, 1978; *Armijo et al*., 1986]. Southern Tibet, the largest high-elevation region on Earth, created by the ongoing India-Eurasia collision, has also experienced a number of normal-faulting crustal earthquakes. In the past four decades, normal-faulting earthquakes have released about 15–20% of the total extensional strain of the Tibetan Plateau, corresponding to 13% of the total moment released for this time period from earthquakes occurring within the plateau with elevations > 4.5 km [*Elliott et al*., 2010]. Some of the clusters of events were triggered by static stress increases from previous nearby earthquakes, e.g., Nima-Gaize [*He and Peltzer*, 2010] and Zhongba sequences [*Elliott*, 2009; *Ryder et al*., 2012]. Studying normal earthquakes in southern Tibet is not only important for understanding regional tectonics [e.g., *Taylor and Yin*, 2009; *Searle et al*., 2011], but also more generally for understanding the structure and dynamics of the lithosphere [e.g., *Jackson and White*, 1989; *Wernicke*, 1995; *Buck*, 2007; *Collettini*, 2011].

The ~350 km long Pumqu-Xainza Rift (PXR, also known as Jiagang-Dinggye Rift) is one of the major rift systems in southern Tibet. The northernmost part of the rift is at Jiagang Snow Mountain, Xainza County (~30.8°N, 88.7°E) where it intersects the right-lateral Gyaring Co fault. At Xaitongmoin County (~29.4°N), the rift is intersected by the Yarlung-Tsangpo Suture. Then it extends southward again to the Pumqu River

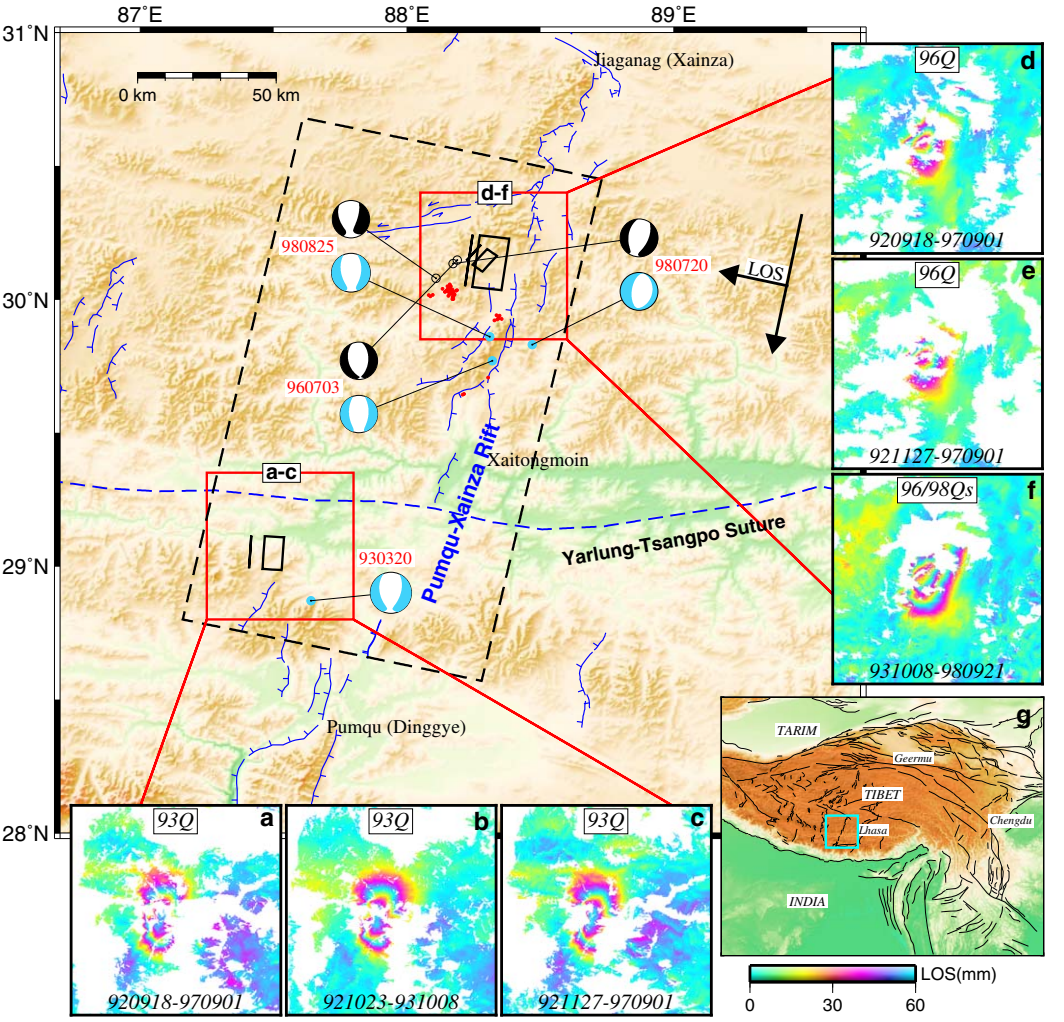

Figure 1. Topographic and tectonic map of the Pumqu-Xainza Rift, southern Tibet, and the observed coseismic radar interferograms. Tick marks on the rifts indicate hanging wall slip direction with faults from *Kali* [2010]. The dashed box delimits the extents of our radar data. The short and long arrows indicate radar looking and flight directions respectively. The colored circles and the "beach-balls" show the locations and the focal mechanisms of the four events from the GCMT (cyan) and NEIC (black) models respectively. The black boxes show the surface projections of InSAR-derived east-dipping fault models, with solid lines representing the fault trace. Red dots denote epicenters of the manually located earthquakes, which occurred in 2004–2005, from *Monigle et al.* [2012]. Portions of the coseismic interferograms in the red boxes are shown in Figures 1a–1c and 1d–1f respectively. Each fringe represents 60 mm of displacement in the satellite line of sight in these rewrapped interferograms. (g) Tectonic map of the Tibetan Plateau with faults from *Taylor and Yin* [2009]. Cyan box indicates the area of the main figure.

at Dinggye County (~28.3°N, 87.7°E) [*Armijo et al.*, 1986; *Kali*, 2010] (Figure 1). Recently, *Monigle et al.* [2012] studied microearthquakes that occurred near Xaitongmoin County between 2004 and 2005 using data from the HiCLIMB experiment. From the locations and mechanisms of these earthquakes, they suggest that active deformation is occurring on low-angle normal faults in this region. Although low-angle normal faults (LANFs, dip $<30°$) were inferred in the shallow crust in the Yadong-Gulu and Lunggar rifts using surface geological information [*Cogan et al.*, 1998; *Kapp et al.*, 2008], no other evidence exists that indicates low-angle normal faults are active in Tibet from geodetic and seismological data [e.g., *Jackson and White*, 1989; *Elliott et al.*, 2010].

As well as previously studied microearthquake swarms [*Langin et al.*, 2003; *Monigle et al.*, 2012], a sequence of four M_w 5.5+ earthquakes occurred in the PXR in the 1990s, with no comparable event occurring since 2000 (Figure 1). The first of the four earthquakes occurred on 20 March 1993 at the southern PXR. The following three events were clustered at the northern PXR near Xaitongmoin County on 3 July 1996, 20 July 1998, and 25 August 1998. This earthquake sequence offers a good opportunity to explore the geometry and mechanism of rifting and to test models of stress transfer and earthquake triggering.

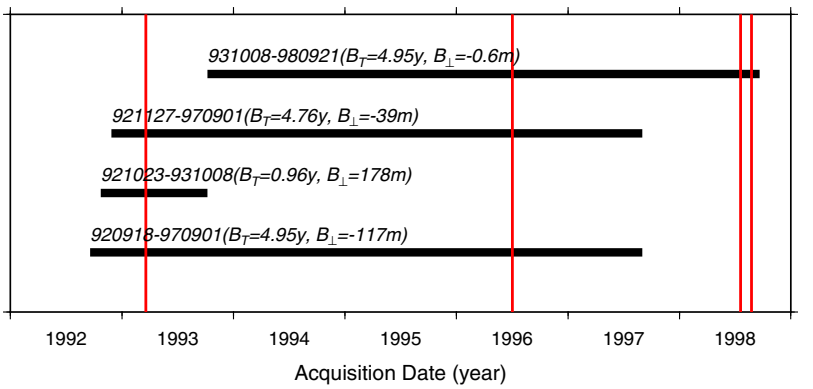

Figure 2. Temporal (B_T) and perpendicular ($B_\perp$) baselines of the interferometric pairs (yymmdd-yymmdd) shown in Figures 1a–1f. The red bars mark the times of the four events studied in this paper.

Interferometric Synthetic Aperture Radar (InSAR) can be used to measure large-scale surface deformation with millimeter-level accuracy and meter-level spatial resolution across the land surface [e.g., *Massonnet and Feigl*, 1998; *Bürgmann et al*., 2000]. Such high-resolution measurements can determine shallow continental fault locations more precisely than seismological methods, and often can resolve the focal plane ambiguity for moderate to large-size earthquakes [e.g., *Biggs et al*., 2006; *Elliott et al*., 2010; *Weston et al*., 2012]. In this paper, we use InSAR, combined with body-wave seismology, to determine the fault parameters of the four M_w 5.5+ earthquakes that occurred in the PXR in the 1990s and investigate possible interactions between these events. We explore the implications for the mechanism of rifting in Tibet. The results potentially have important implications for the distribution of seismic hazard in extensional zones worldwide.

2. InSAR Data and Modeling

2.1. InSAR Data Processing

Only ESA's ERS-1/2 satellites acquired radar data suitable for measuring the coseismic deformation associated with the four earthquakes in the PXR. We use the JPL/Caltech ROI_PAC software [*Rosen et al*., 2004] to process the ERS-1/2 radar acquisitions from descending track 491. The topographic phase is removed using Delft precise orbits [*Scharroo and Visser*, 1998] and the 3 arc-s (~90 m) DEM from the Shuttle Radar Topography Mission (SRTM) [*Farr et al*., 2007]. The interferograms are filtered using a power spectrum filter [*Goldstein and Werner*, 1998] and unwrapped using a branch-cut method [*Goldstein et al*., 1988]. Phase unwrapping errors are manually corrected. Finally, we select the best four interferograms with reasonable coherence for the following analysis. Figure 2 shows the interferometric pairs used, along with their temporal and spatial baselines.

We fit orbital and topography-correlated atmospheric delay errors for each interferogram by masking the coseismic displacements. The orbital errors are fit using a linear function of x and y coordinates, and the atmospheric delay errors are fit using a linear relationship between far-field displacements and elevation [e.g., *Elliott et al*., 2008]. Figures 1a–1f show observed coseismic deformation for the two source areas from a variety of image-pairs.

Both the 1993 and 1996 events are covered by three interferograms as shown in Figures 1a–1c and 1d–1e respectively. Because the interferograms associated with each event have almost identical looking geometry, joint inversion with multiple interferograms will not help constrain the models. So we invert fault parameters based on stacked interferograms for these two events separately (Figures 3a and 3b). The interferogram 931008–980921 covers three events (Figure 2). We subtract the contributions of the 1996 event (Figure 3b) and obtain displacements associated with events 980720 and 980825 (Figure 3c).

2.2. InSAR Modeling

It is impractical to model the faulting using millions of data points yielded in a single interferogram. Instead, we use a quadtree algorithm to downsample the interferograms [e.g., *Jónsson et al*., 2002; *Simons et al*.,

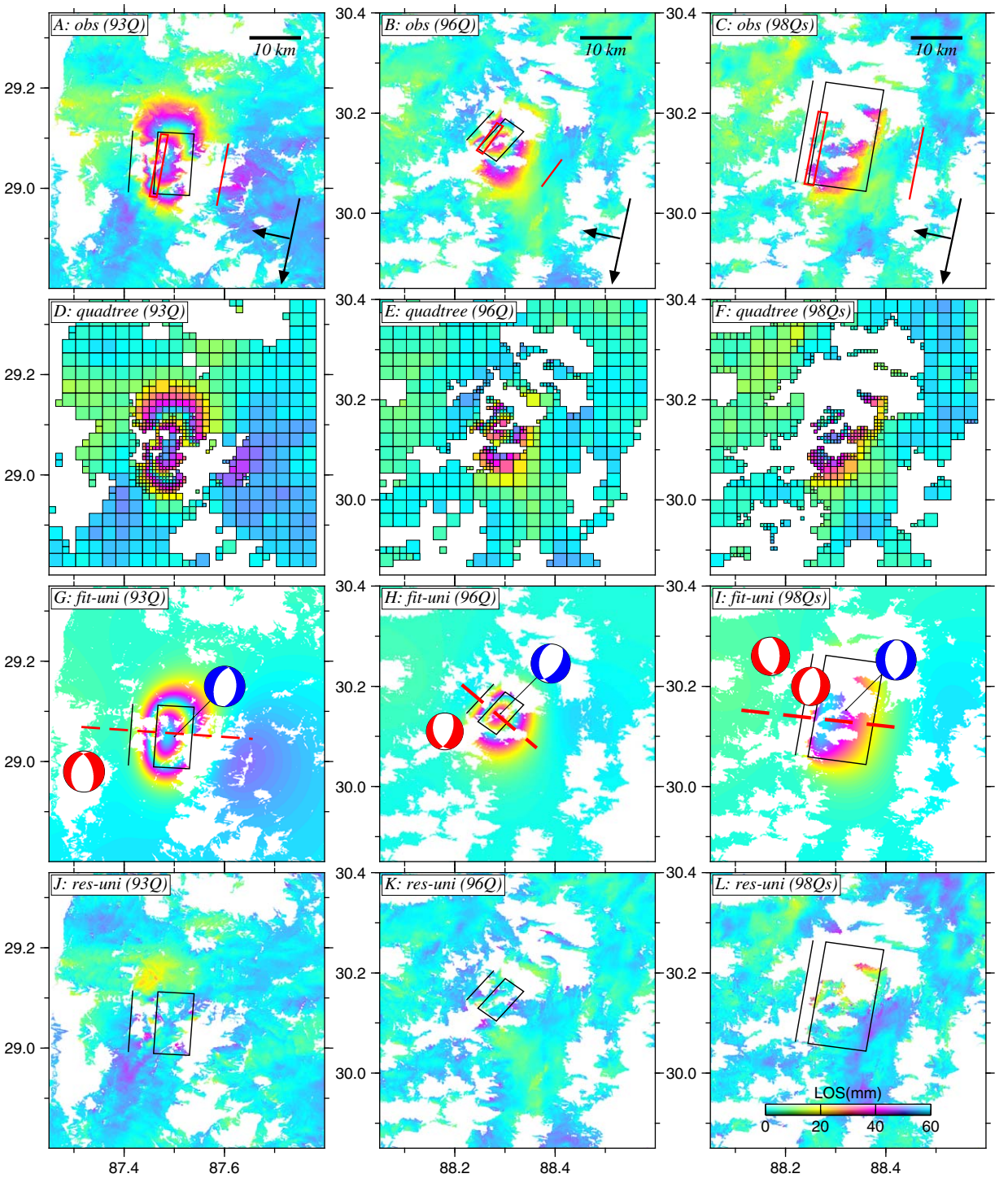

Figure 3. Stacked coseismic displacements and uniform slip modeling. (a) Coseismic interferogram for the 1993 event stacked using data in Figures 1a–1c. (b) Coseismic interferogram for the 1996 event stacked using data in Figures 1d and 1e. (c) Coseismic interferogram for the 1998 events using the difference between Figures 1f and 3b. The black and red boxes show the surface projections of the east and west-dipping fault models respectively, with solid lines representing the fault trace. The short and long arrows indicate radar looking and flight directions respectively. (d–f) Down-sampled observations using quadtree algorithm. (g–i) Synthetic interferograms from the east-dipping uniform slip models. The "beach-balls" denote focal mechanisms from BW (red) and ICMT (blue) solutions. (j–l) Residuals from the east-dipping uniform slip models.

2002], which usually gives denser measurements in the near field where the deformation gradient is higher than the far field. The resulting dataset consists of about 600 data points for each interferogram (Figures 3d–3f).

We determine source parameters of the normal earthquakes using a rectangular dislocation model in a homogeneous elastic half-space [*Okada*, 1985]. We also solve a linear function of x and y coordinates to remove the residual orbital errors. In the dislocation model, the parameters defining the fault geometry have nonlinear relationships with surface displacements. To solve this nonlinear optimization problem, we use a simulated annealing algorithm followed by a quasi-Newton method [*Cervelli et al*., 2001]. The simulated annealing method locates the valley that contains the global minimum of misfit, then a quasi-Newton method finds the bottom of that valley and gives the best-fit solution. We assume the opening is zero and all the other fault parameters are freely variable. The best-fitting model minimizes the weighted misfit between the data and model predictions. We estimate the weight matrices using far-field measurements in the stacked interferograms based on a 1-D covariance function [*Parsons et al*., 2006]. We take the same Poisson's ratio ($\nu = 0.25$) as used by *Elliott et al*. [2010], based on crustal seismic velocities of $V_P = 6.0$ km s^{-1}, $V_S = 3.45$ km s^{-1}, $\rho = 2780$ kg m^{-3} [*Steck et al*., 2009].

We estimate the uncertainties of the fault parameters using a Monte-Carlo simulation technique [e.g., *Lohman and Simons*, 2005; *Parsons et al*., 2006]. We construct 100 simulations of spatially correlated random noise based on the variance-covariance matrix for each interferogram. The observed data are then perturbed by adding the simulated noise. We invert the perturbed data and obtain a set of 100 model solutions (Figures 4 and supporting information Figures S1–S3). The uncertainty of each fault parameter can be estimated from its distribution in the model solutions. Fault parameters other than slip have a nonlinear relationship with surface displacements [*Okada*, 1985], and trade-offs have commonly been observed between the fault parameters in geodetic inversions [e.g., *Wright et al*., 2003, 2004; *Funning et al*., 2005; *Ziv et al*., 2013]. InSAR only measures 1-D line-of-sight deformation, which aggravates the trade-offs. The Monte-Carlo simulations plotted in Figure 4 also display trade-offs in some cases. There are strong positive or negative correlations between fault depth, width, strike, dip, and slip for the 1993 earthquake. Some trade-offs have simple explanations. For example, decreasing the fault width reduces the modeled surface deformation and hence the slip increases to compensate. To validate the trade-offs, we estimate the trade-off expected when linearizing the model about the best-fitting solution, in a semianalytical way. To achieve this, we calculate partial derivatives of displacement with respect to each model parameter, following *Feigl and Dupré* [1999]. We then use these to populate the Jacobian of the forward model (J), and propagate the errors in the data variance-covariance matrix (C_d), to give the model variance-covariance matrix, $C_m = (J' C_d^{-1} J)^{-1}$. The red lines in Figure 4 show the direction of correlation for each pair of parameters from the resulting model variance-covariance matrix. We find that our results generally agree well with that derived by propagation of data errors. All fault parameters and their 1-σ uncertainties are listed in Table 1 and named as ICMT, i.e., InSAR CMT. Overall, the uncertainties are relatively small and the moment magnitude, dependent on the fault area times the slip, remains roughly constant despite the parameter trade-offs.

The 1993 and 1996 events can be fit well using a single rectangular dislocation model (black rectangles in Figures 3g and 3h). The RMS residuals are 6 mm and 4 mm respectively (Figures 3j and 3k), comparable to the uncertainties of 5 and 6 mm estimated by the 1-D covariance function fit to the far-field data. Figure 3c comprises coseismic deformation due to the 1998 events. It is not possible to separate these two events and we model the combined deformation as having occurred on a single fault plane. The rake is poorly constrained with 1-σ error of 33° (Table 1). After fixing the rake to the average of the 1998 events from body-wave solutions, the uncertainty of strike becomes smaller while the other parameters are not significantly different (Table 1). In the rest of the paper we will use the fixed-rake solution. The resultant model gives a RMS of 6 mm, the same as the uncertainties of the measurements (Figure 3l). All the models give small orbital errors with the maximum of 0.04 mm/km in east and 0.08 mm/km in north, as we have already removed most of the orbital errors using a far-field planar correction.

We further subdivide the fault plane into patches and estimate the slip distribution, which has been routinely used to model large earthquakes [e.g., *Jónsson et al*., 2002]. However, our distributed slip models do not significantly improve the goodness of fit (supporting information Figures S4–S6). In particular, the majority of slip is found to be inside the rectangular uniform-slip plane for all the events (supporting information Figures S7–S9). Therefore, we conclude that our single-fault uniform slip models are good enough for these moderately sized earthquakes.

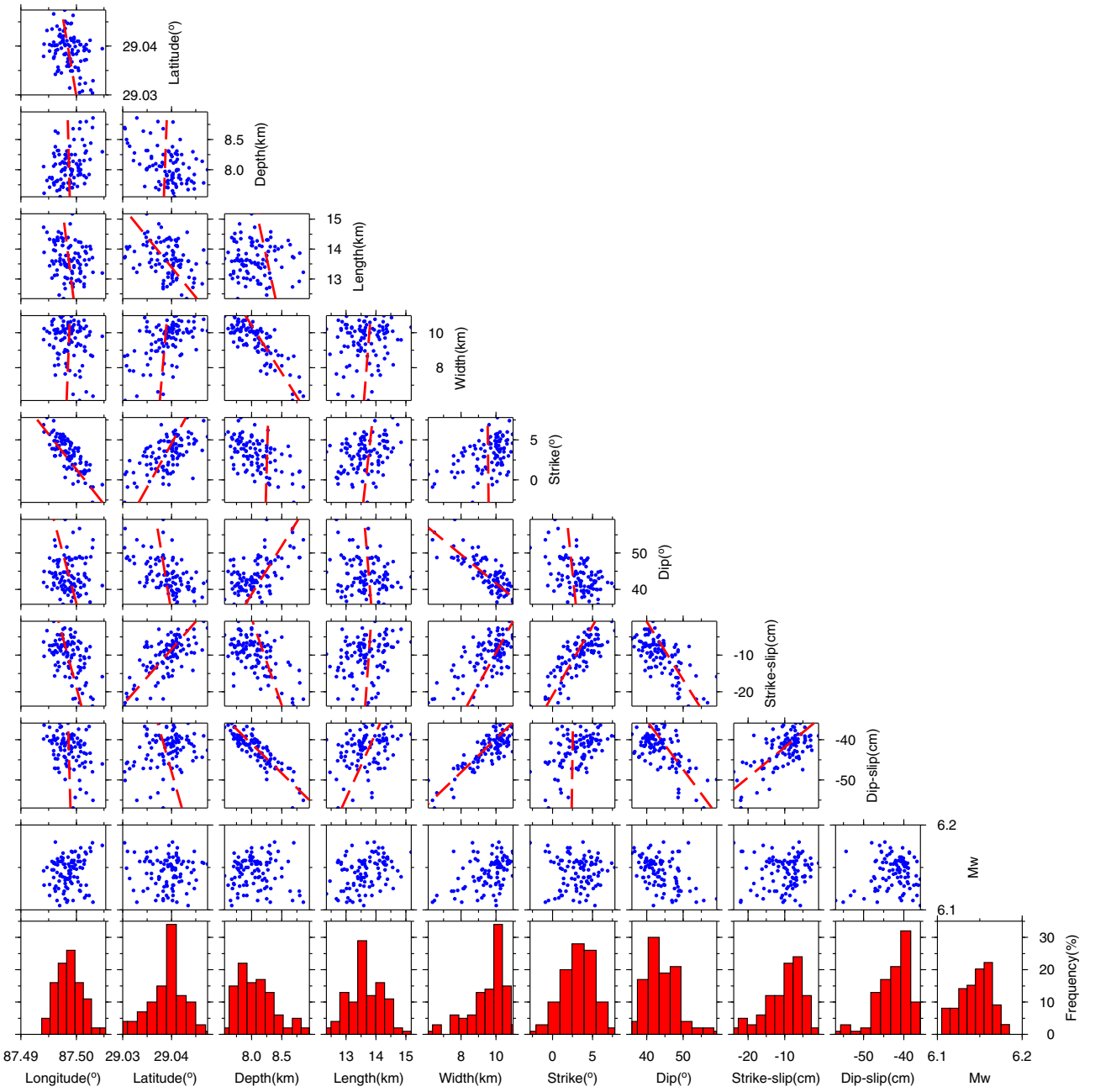

Figure 4. Model parameters of the 1993 event computed using the Monte-Carlo simulation technique. Histograms show distribution in individual model parameters. The dashed red lines show trade-offs between pairs of model parameters using a semianalytical approach.

3. Teleseismic Body-Wave Modeling

We determine source parameters for the earthquakes that have occurred along the Pumqu-Xainza rift using teleseismic body-wave seismology, for comparison to our InSAR results. Seismograms were retrieved from the IRIS DMC, principally using data from the Global Digital Seismograph Network (GDSN). We use stations within an epicentral distance of 30–90° for *P* waves and 30–80° for *SH* waves, allowing us to ignore the influence of regional head-waves or mantle triplications on the waveform. Broadband data were filtered to extract periods between 15 and 100 s, limiting the influence of fine-scale velocity structure on the waveforms, and allowing the earthquake source to be treated as the finite-duration rupture of a point source, for the magnitude of the earthquakes involved in this study.

Table 1. Fault Parameters From InSAR (ICMT), Body-Wave Modeling (BW), and as Listed in the GCMT and NEIC Catalogs

Model	Longitude[a] (°)	Latitude[a] (°)	Depth[a] (km)	Strike (°)	Dip (°)	Rake (°)	Length (km)	Width (km)	Slip (cm)	M_0 (10^{18}N*m)	M_w
20 Mar1993 Event											
GCMT	87.64	28.87	15	161(22)	46(52)	−121(−62)				2.47	6.2
BW	87.321	28.983	8	346(198)	55(40)	−110(−64)				1.67	6.1
ICMT	87.499	29.049	8	4	43	−102	13.6	9.7	43	1.81	6.14
ICMT(1-σ)	±0.002	±0.004	±0.3	±2	±5	±5	±0.6	±1.1	±5	±0.12	±0.02
3 Jul 1996 Event											
NEIC	88.189	30.147	5	161(7)	44(49)	−109(−72)				0.35	5.7
GCMT	88.32	29.77	15	172(8)	45(46)	−102(−78)				0.35	5.7
BW	88.177	30.107	7	20(161)	58(39)	−67(−122)				0.29	5.6
ICMT	88.292	30.146	7	39	54	−65	8.4	7.8	44	0.93	5.95
ICMT(1-σ)	±0.003	±0.003	±0.6	±6	±9	±6	±0.7	±3.1	±12	±0.15	±0.04
20 Jul 1998 Event											
NEIC	88.173	30.134	5	29(181)	51(43)	−72(−111)				0.52	5.8
GCMT	88.47	29.83	15	16(187)	32(59)	−83(−95)				0.48	5.8
BW	88.253	30.196	7	9(192)	49(41)	−92(−88)				0.49	5.8
25 Aug 1998 Event											
NEIC	88.109	30.079	11	24(144)	64(44)	−53(−141)				0.37	5.7
GCMT	88.31	29.86	15	14(162)	46(48)	−67(−112)				0.68	5.9
BW	88.168	30.259	10	1(158)	51(41)	−75(−108)				0.45	5.7
ICMT-freerake[b]	88.315	30.139	8	7	46	−113	21.6	15.4	14	1.49	6.09
ICMT(1-σ)	±0.010	±0.054	±1.0	±22	±7	±33	±2.9	±2.1	±3	±0.21	±0.04
ICMT-fixedrake[b]	88.320	30.153	8	9	45	−83	22.7	16.0	12	1.44	6.08
ICMT(1-σ)	±0.010	±0.030	±0.8	±13	±8	fixed	±2.1	±2.6	±2	±0.22	±0.05

[a]The location (longitude, latitude and depth) refers to the centroid, except in the case of the BW entry, which is the epicenter (longitude, latitude) taken from the EHB catalog [*Engdahl et al*., 1998].

[b]This model comprises displacements due to the 1998 pair of events.

P and *SH* waves were then jointly inverted using the method of *Zwick et al*. [1994] to determine the focal mechanism, centroid depth, moment and source-time function based on the waveform shape and amplitude over a window encompassing the direct arrival (*P*, *S*) and the principal depth phases (*pP*, *sP*, *sS*). Starting parameters for the inversion were taken from the GCMT catalog and the source is constrained to be a pure double-couple. The start-time of the inversion window for each seismogram is manually picked based on the arrival of the relevant direct phase on the broadband seismogram. We use a source-side velocity structure consisting of a half-space consistent with the elastic half-space used in calculating near-source displacements during InSAR inversion.

An example, for the 1996 event, is shown in Figure 5. Minimum misfit solutions are listed in Table 1 and named as BW. The method employed here has been used extensively in previous studies [e.g., *Molnar and Lyon-Caen*, 1989; *Sloan et al*., 2011]. Typical errors in strike and rake at ± 10°, and depth ±3 km [e.g., *Molnar and Lyon-Caen*, 1989; *Taymaz et al*., 1990].

4. Discussion

The study of the geometry and location of normal faulting is important for understanding the extension of the continental crust [*Jackson*, 1987] and for understanding the mechanics of faulting [*Collettini and Sibson*, 2001]. Such studies can also help resolve debates concerning active low angle normal faults [*Axen*, 2007] and the cause of the east-west extension in Tibet [e.g., *England and Houseman*, 1989; *McCaffrey and Nabelek*, 1998; *Yin*, 2000; *Kapp and Guynn*, 2004]. Comparing recent earthquakes with evidence of active faulting allows us to test the relationship between earthquake size and surface expression [*Dawers et al*., 1993] and to potentially determine rates of extension based on topography, because large normal faulting events contribute most to the seismic moment release [*Scholz and Cowie*, 1990]. Detailed studies of normal faulting earthquakes have been limited in the past and, to date, previously studied ruptures with InSAR number just slightly more than 20 events [*Wright et al*., 2013]. However, observations of ground deformation using satellite interferometry associated with such events permit a more accurate determination of fault locations and geometry than previously possible, particularly where a surface rupture is absent. In this study, we have examined the relationship of moderate normal faulting with topography and the overall rift structure in the Pumqu-Xainza Rift of southern Tibet, as well as determining reliable fault plane dips and verifying these observations against seismological solutions.

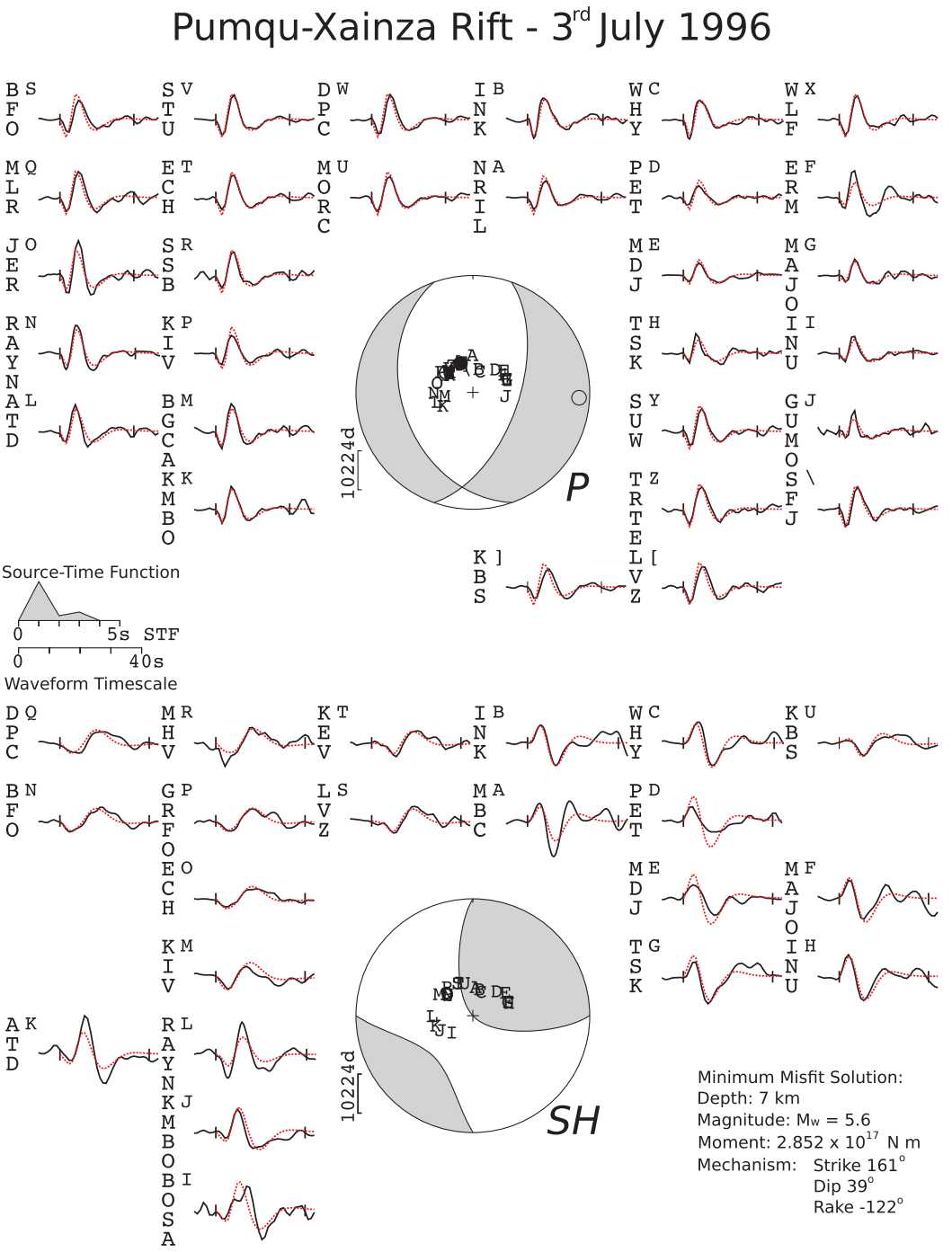

Figure 5. Teleseismic waveform modeling solution for the earthquake on 3 July 1996. The method used is described in the text. Data are shown in black, synthetics for the minimum misfit solution shown in red. Spheres show lower hemisphere projections of the radiation patterns. Upper sphere and waveforms are for *P* waves, lower sphere and waveforms are *SH* waves.

4.1. Comparison of InSAR and Seismological Models

Table 1 shows that InSAR and body-wave models derive consistent fault geometry parameters including centroid depth, strike, dip and rake. The centroid depths particularly agree with each other for the 1993 and 1996 events. All our models suggest that these earthquakes occurred with centroids no deeper than 10 km, and hence are located in the seismogenic upper crust. The deeper centroid estimates from the GCMT catalog are due to the difficulty in determining the depths of such shallow earthquakes from very long-period body and surface waves. The rakes show that these earthquakes are mainly dip-slip with a small component

of strike-slip. Of particular interest to this study is the uncertainty in the dip of the fault planes, which is discussed in detail later.

InSAR provides high-resolution deformation measurements in the epicentral area, ensuring an advantage over seismology in determining precise earthquake locations for moderately sized earthquakes in shallow continental areas [*Weston et al*., 2012; *Wright et al*., 2013]. Making comparisons with the InSAR models, the GCMT [*Ekström et al*., 2012] and EHB [*Engdahl et al*., 1998] locations have biases of 24 km SE and 19 km SW for the 1993 event; the biases for the 1996 event are 42 km SSE, 10 km and 11 km to the west for the GCMT, NEIC and BW solutions respectively. *Elliott et al*. [2010] typically found GCMT locations of normal earthquakes across Tibet biased 15–30 km to the SSE and NEIC locations 0–15 km to the SSW. Such offsets are mainly due to relatively poor data coverage and the velocity structure used in seismology.

The moment magnitude of the 1993 event is consistent between InSAR and body-wave models. The InSAR-derived moment for the combined 1998 pair is higher than the sum of the seismological solutions by $\sim$50%, with potential postseismic motion from the 1996 and 1998 earthquakes contributing to this difference. For example, a M_w 5.4 aftershock on 21 July 1998 contributed more than 10% of the difference although it can not be constrained as well as the other earthquakes using body-wave data. Additionally, a large discrepancy occurs for the 1996 event itself—the InSAR determined moment lies well beyond the uncertainty of the body-wave model, although the geometrical parameters agree well. Considering that both interferograms used in our model spanned about 5 years for the 1996 event, we suggest that postseismic deformation is also the most likely mechanism to explain the larger moment magnitudes of ICMT although we can not completely exclude the effect of atmospheric artefacts in InSAR observations.

Our InSAR models give fault lengths of 13.6$\pm$0.6 and 8.4$\pm$0.7 km for the 1993 and 1996 events respectively, which can be solved unambiguously, consistent with the scaling law of normal earthquakes estimated by *Wells and Coppersmith* [1994], i.e., $M_w = 4.34 + 1.54 \log(L)$. The single-fault plane used to model the 1998 pair of events is longer than the others although the total moment is still smaller than the 1993 event. It may imply that the two 1998 earthquakes occurred successively from south to north, as suggested from locations in the EHB epicenters (Figure 1) and the two concentrated patterns of the slip distribution model (Figure S9a), but it is not possible to resolve the exact spatial relationship with respect to the 1996 event.

4.2. Dip Angle

A long-term debate on low-angle normal faults is whether or not such faults are active in the seismogenic crust [e.g., *Jackson and White*, 1989; *Wernicke*, 1995; *Axen*, 2007; *Abers*, 2009; *Collettini*, 2011]. Standard Anderson-Byerlee fault mechanics predicts that it is easier to form or reactivate a normal fault in the dip range 30–60° than reactivate an existing LANF [*Anderson*, 1942; *Byerlee*, 1978; *Collettini and Sibson*, 2001]. 30–60° is also the typically observed range for active faults [*Jackson and White*, 1989; *Thatcher and Hill*, 1991; *Sibson and Xie*, 1998; *Collettini and Sibson*, 2001]. Possible mechanics for seismic activity on LANFs are (i) stress field rotation or (ii) low friction relative to laboratory values due to weak materials or high fluid pressure in fault zones [*Axen*, 2004; *Abers*, 2009]. Whilst the fracture strength of the material may be well constrained in the laboratory, the effective failure strength on a geological scale remains uncertain, especially in a region with pre-existing structures [*Middleton and Copley*, 2014]. It is also hard to explain the absence of major earthquake on LANFs over tens of years [*Jackson and White*, 1989; *Collettini and Sibson*, 2001; *Collettini*, 2011; *Elliott et al*., 2010]. High-resolution InSAR measurements are able to resolve the ambiguity of focal planes. Analyzing eight normal-faulting earthquakes in Tibet using InSAR and body-wave inversion, *Elliott et al*. [2010] identified that all the faults have moderate dips peaking at 45°, and some of them are not associated with surface geomorphology.

In this study, all the interferograms in Figure 1 show higher phase gradients on the western side of the fringe pattern, implying an east-dipping fault plane. Our optimal ICMT models require dips of $43^\circ, 54^\circ, 45^\circ$ (Table 1), confirming our analysis of deformation patterns. Figure 6 shows the dip/misfit curves for the seismologically determined solutions, and demonstrates that all InSAR-estimated dips are consistent to within 2σ uncertainties of the nodal planes of the seismological focal mechanisms for all four earthquakes. Of particular interest is the 1996 event whose epicenter is near the micro-earthquakes in *Monigle et al*. [2012]. Our models provide its dip of 54° (ICMT) and 58° (BW), consistent with the high-angle solution (61°) in *Monigle et al*. [2012]. We note that the dip estimates for the east-dipping plane in the 1993 event derived independently from InSAR and seismological data differ by $\sim$10 degrees. This may represent some degree of

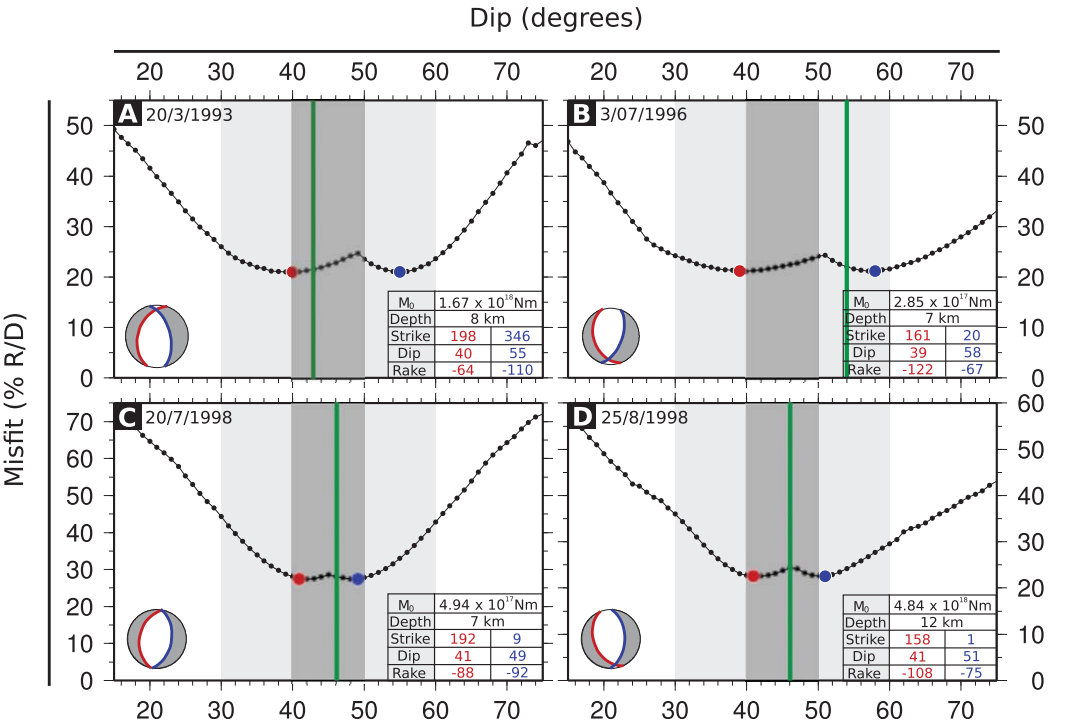

Figure 6. Dip versus misfit plots for the four earthquakes. In each plot, dip is fixed at 1° intervals, and a best-fit source mechanism determined with all other parameters free to vary. Colored circles indicate the two nodal planes of the global minimum misfit solution, which is also indicated by the table, and the focal mechanism on each plot. Green bars indicate the dip determined by inversion of the InSAR data. Misfit is represented as a percentage of the residual over the data amplitude at each sampling point. Gray shaded boxes in the background highlight dip ranges.

complexity in either the source geometry or elastic structure that we are unable to constrain with the available data, when using a single-fault or point-source model in a half-space. However, neither technique requires the fault to be active at angles of $< 40°$.

In order to test if the earthquakes could possibly be associated with west-dipping planes, we redetermined the source models while constraining their strikes as between 120° and 240°. The west-dipping models can fit the data almost equally well, but all of them require an extremely small down-dip width ($\sim$ 1 km) and high slip (the upper bound of 2 m). This implies that a linear source is preferred, which is inconsistent with fault scaling laws [*Wells and Coppersmith*, 1994]. Furthermore, these linear-source models approach the top of the east-dipping fault planes following the high-gradient surface deformation (red boxes in Figures 3a–3c). These lines of evidence help us rule out the west-dipping low-angle planes for the earthquakes in the PXR. Although we studied different earthquakes, our data strongly suggest that the occurrence of major seismicity on the low-angle plane inferred by *Monigle et al.* [2012] is questionable.

4.3. Stress Transfer

We have examined the potential triggering relationship between these successive events in the Pumqu-Xainza Rift by calculating the Coulomb stress change on each of the fault segments based upon their relative positions and geometry as determined by the InSAR observations. Receiver geometries for the other mapped faults in the area are assumed to be dipping at 45° and have a pure normal rake. We use Coulomb 3.1 to derive the static stress changes associated with these earthquakes [*Lin and Stein*, 2004]. We assume an effective coefficient of friction of 0.4 and a shear modulus of 3.2×10^{10}Pa to match that used in the InSAR and body-wave modeling.

We take the uniform slip solution for the M_w 6.2 20 March 1993 event and determine the change in Coulomb stress on receiver faults with the same orientation as the 1996 event (supporting information Figure S10). Despite being along-strike from the first event, given the relatively small magnitude of the earthquake compared to the 150 km separation between these events, the static stress changes are negligible at this

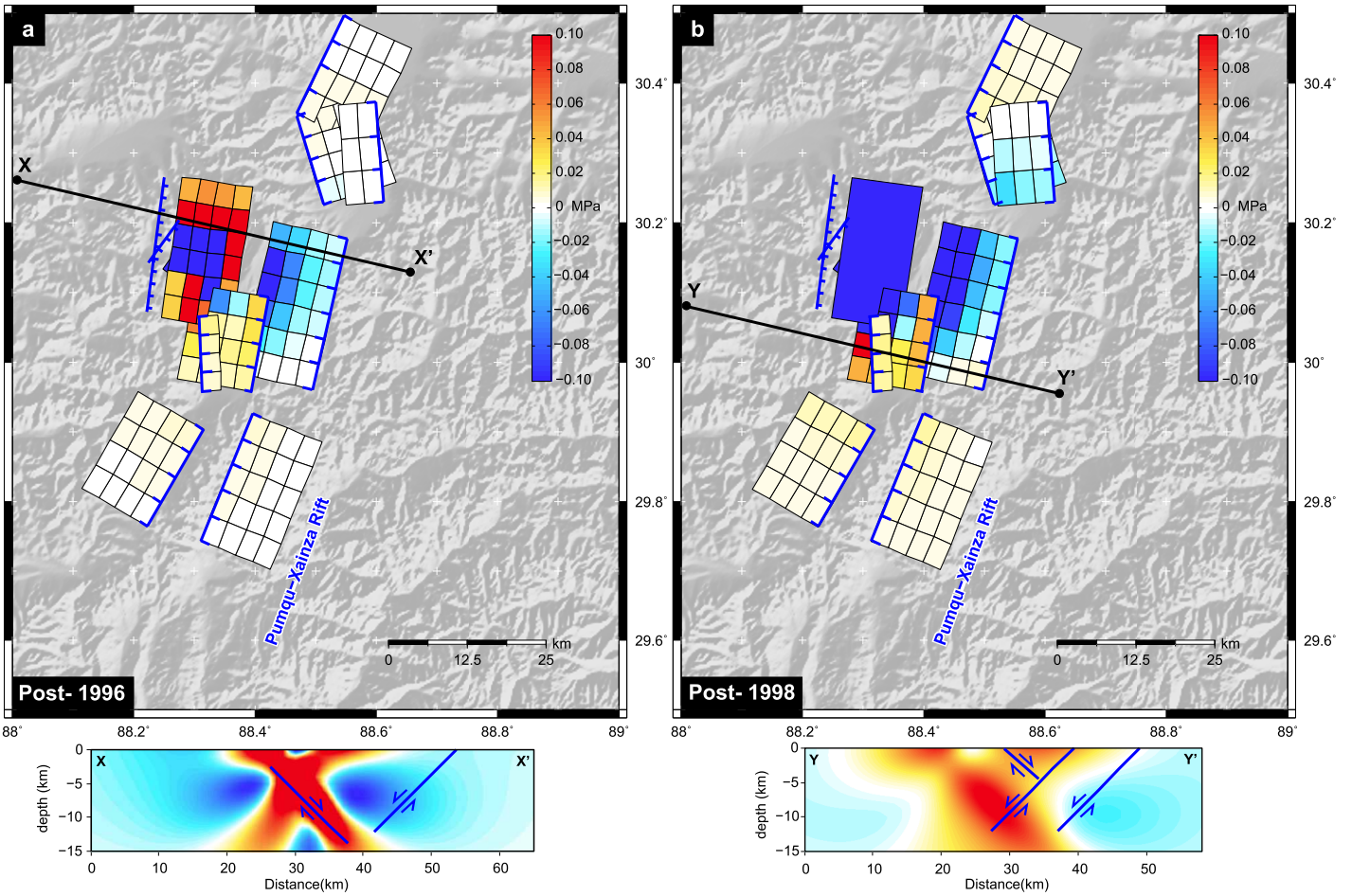

Figure 7. Coulomb stress change on the Pumqu-Xainza Rift faults surrounding the 1996 and 1998 fault ruptures, calculated using Coulomb 3.1 [*Lin and Stein*, 2004] and based upon the InSAR uniform slip models (other faults in the region are assumed have a 45° dipping plane with pure normal slip and a simplified fault geometry aligned with the mapped surface trace). The color range has been saturated at ±0.1 MPa to highlight the stress change on other faults. (a) Coulomb stress change on faults resulting from the 1996 M_w 5.9 earthquake. The profile X–X′ shows the stress changes for receiver faults with the geometry of the 1998 fault plane. (b) Coulomb stress change on faults resulting from the combined effect of the 1996 M_w 5.9 earthquake and the 1998 M_w 5.8 pair. The profile Y–Y′ shows the stress changes for receiver faults with the geometry of the westward dipping fault planes.

distance. There are, however, significant increases in stress along strike on mapped faults to the immediate south of this fault rupture (Figure S10).

However, for the interaction between the 1996 and pair of 1998 events, their close proximity makes the Coulomb stress changes much more significant, despite being Mw 5.7–5.8 events. The stress change calculated on the subfault patches for the combined 1998 fault geometry is shown in Figure 7. The 1996 earthquake reduces the static stress in the center of the assumed 1998 fault plane, but increases it at either end. This may support the successive rupture of the July and August 1998 earthquakes at separate ends of the 1996 event.

Regarding other known faults in the vicinity, the stress change has decreased on the segment due east of the 1996/1998 events, but has increased significantly on the westward dipping segment to the south-east (Figure 7b), bringing this closer to failure.

4.4. Fault Geomorphology and Seismic Hazard

The relationship between surface displacements and geomorphology, as recorded in the topography along three profiles for each of the earthquakes, is shown in Figure 8. In each case, the up-dip projection of the InSAR-modeled fault plane to the surface is not correlated with a significant step in the topography associated with a typical graben structure. Comparison of satellite imagery and active fault structures in the two epicentral areas examined (Figure 9) indicates that these earthquakes occurred away from the known and

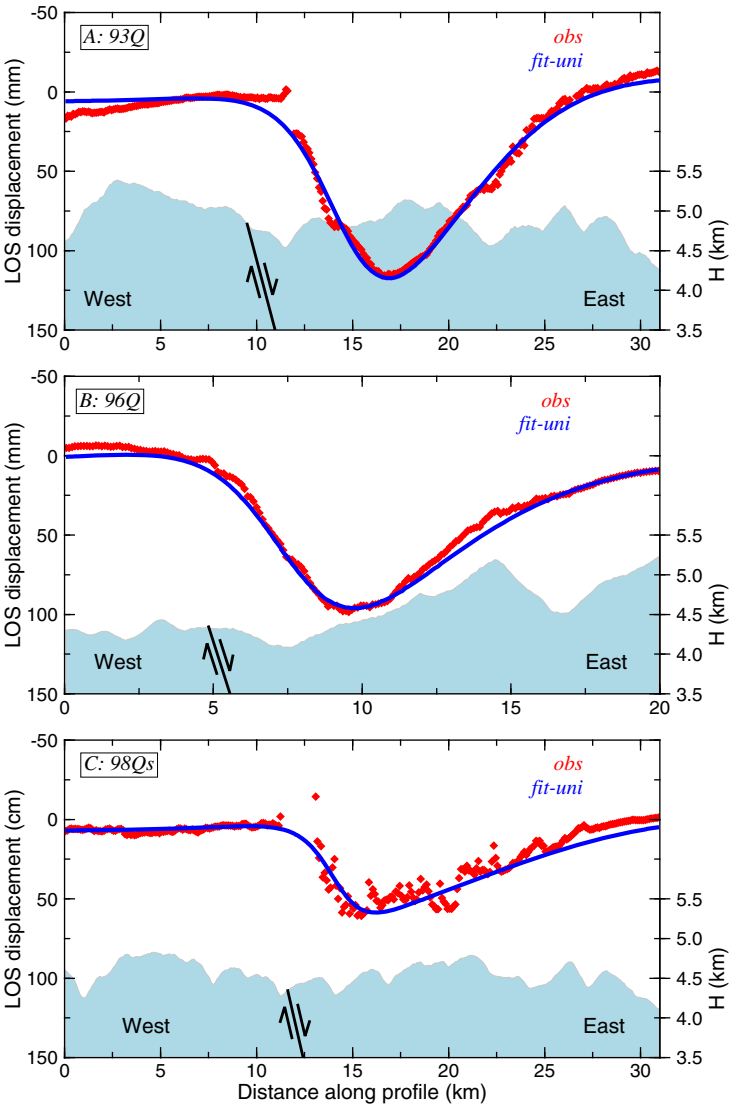

Figure 8. Observed (red) and synthetic (blue) displacements along the profiles which are marked as dashed lines in Figures 3g–3i. Note that positive values indicate motion away from satellite, corresponding to subsidence on the hanging wall for normal earthquakes. The blue bands show elevation along the profiles. The black arrows indicate the slip directions of the normal faulting events. The figure indicates that minimal slip in the earthquakes reached the surface.

previously mapped faults from *Kali* [2010] and, furthermore, that the 1993 Mw 6.2 earthquake occurred in part of the Pumqu-Xainza Rift that does not exhibit a clear expression of active faulting in the surface topography. Predicted subsidence patterns based upon the fault dislocation models for each of these events are not centered on the clear, existing low-relief grabens, but rather are found associated with the higher relief on the western edges of the rift (Figure 10). The east-west lateral extent of active faulting indicates these zones of extension are broader than previously thought, with widths of $\sim$ 50 km—much wider than the surface expression and mapped faults [*Taylor and Yin*, 2009; *Kali*, 2010], which alone indicate perhaps half this width.

The earthquakes studied here suggest that the M5–6 earthquakes do not contribute significantly to build topographic relief, but that they occurred in geologically complex locations. For instance, the 1996/1998 clusters and later swarms in 2004–2005 are located at segment boundary, or hinge, between east-dipping range-front fault to the north, and west-dipping en echelon faults to the south (Figure 1). The 1993 event is in a section where faults themselves are less prominent in geomorphology. One would anticipate complex faulting at these locations.

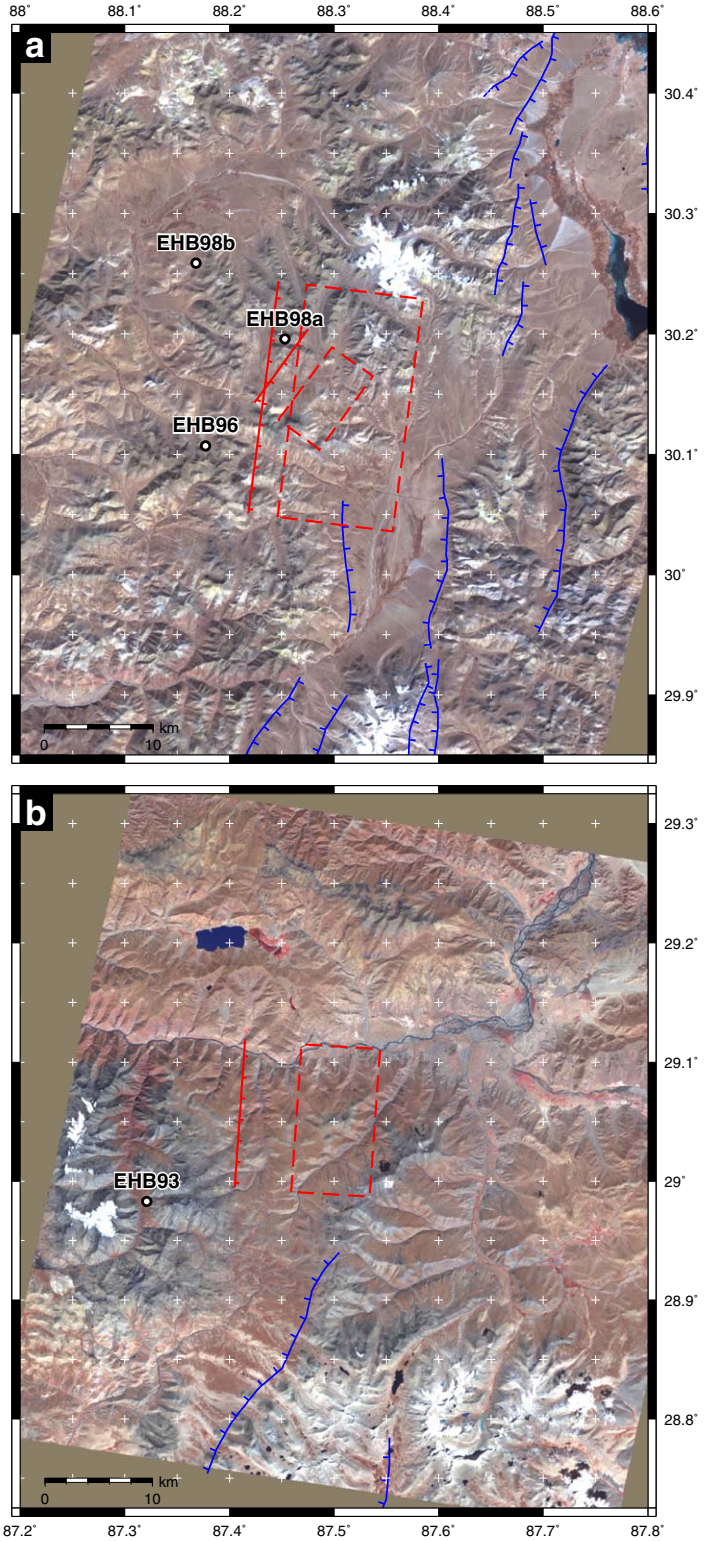

Figure 9. (a) Fault plane locations and up-dip projections to the surface for the uniform InSAR slip models of the 1996 and 1998 earthquake pair (red dashed boxes) overlaid on ASTER satellite imagery (RBG 321). Earthquake epicenters from the EHB catalog [*Engdahl et al.*, 1998] shown as white circles. Other Pumqu-Xainza Rift faults are retraced from *Kali* [2010] (blue lines). The satellite imagery shows the clear geomorphic expression of normal faulting associated with the previously mapped faults. However at this scale, there are no similar topographic expressions associated with any of the 1996–1998 events. (b) Fault plane location for the uniform InSAR slip model for the M_w 6.2 1993 earthquake 150 km to the south of the 1996–1998 events. Here the evidence for rifting is absent in the geomorphology and the up-dip projection of the 1993 fault plane is not associated with any clear scarp in the topography.

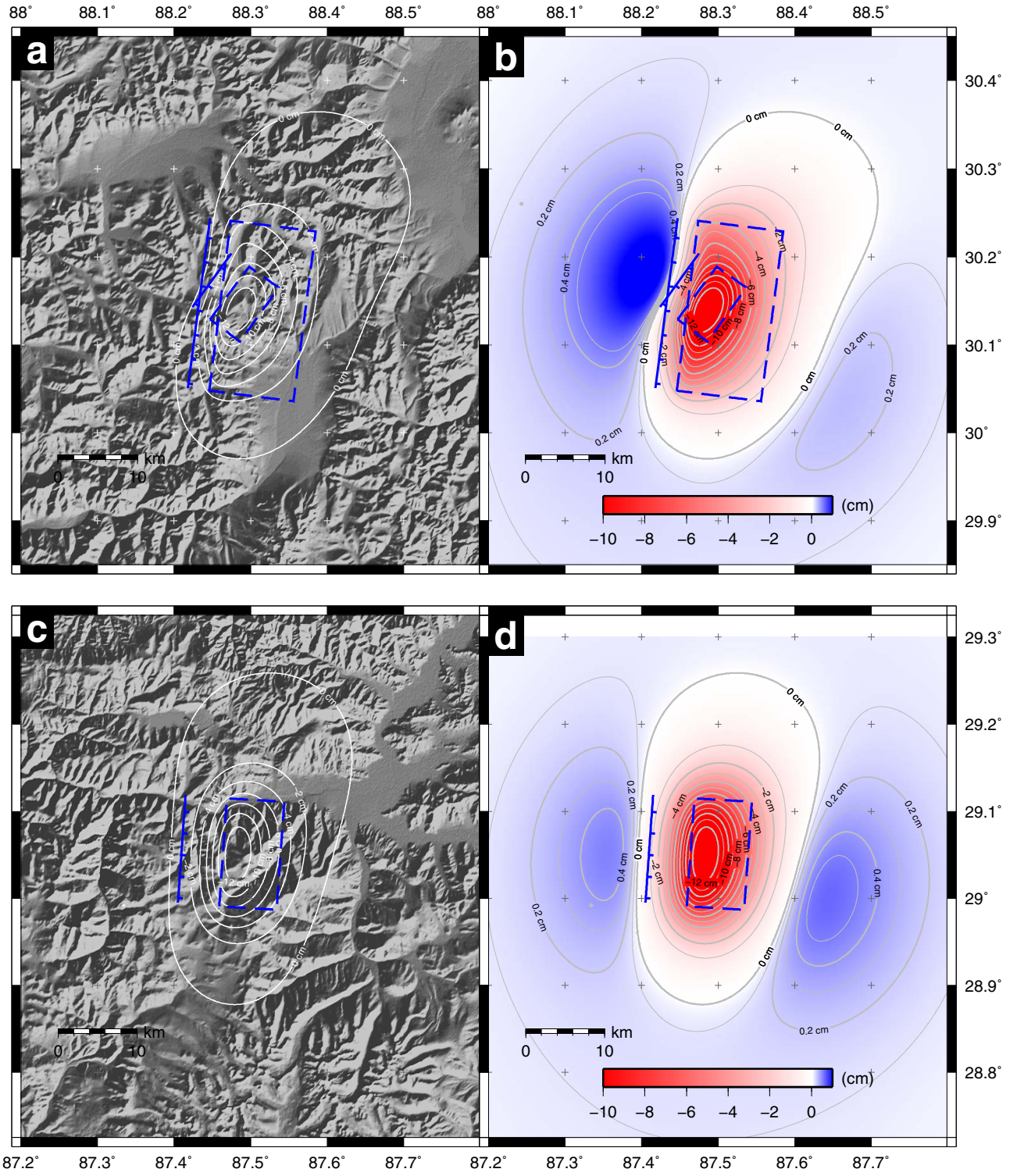

Figure 10. (a) Contours of subsidence from the M_w5.7–5.9 1996 and 1998 uniform slip models overlain on hill-shaded SRTM DEM. (b) Modeled subsidence (red) and uplift (blue) patterns—note the strong asymmetry in relative magnitude of uplift/subsidence used in the color-scale. The subsidence is not centered on the basins. (c, d) Caption as for Figure 10a and 10b but for the 1993 M_w 6.2 event.

In other parts of the world, major normal faults are mostly well mapped in major extensional regions like the Basin and Range province, the Aegean, and the Appennines [*Eaton*, 1982; *Wernicke et al*., 1988; *Anderson and Jackson*, 1987; *Taymaz et al*., 1991; *Jackson*, 1994]. Recent dense GPS measurements show that strain is

distributed throughout these regions instead of merely focusing on the major faults [*Aktug et al*., 2009; *Floyd et al*., 2010; *Nocquet*, 2012; *Hammond et al*., 2014]. This work on southern Tibet also implies that smaller earthquakes can occur away from the major mapped faults. Therefore the seismic hazard could be more broadly distributed than the surface features suggest. Denser geodetic velocity field from GPS and InSAR may lead to better resolution of the deformation and seismic hazard assessment in the extensional regions [*Wang and Wright*, 2012].

5. Conclusions

In this paper, we investigated the coseismic deformation associated with the earthquake sequence that occurred in the Pumqu-Xainza Rift, southern Tibet. Our InSAR results unambiguously demonstrated that all these active normal faults have moderate dip angles (40–60°). None of the surface projections of the fault planes studied here are associated with a step in topography, indicating that it is unreliable to identify focal plane of seismological solutions using surface geomorphology alone. The lateral extent of the earthquake sequence indicates active faulting zones are broader than the surface expression would suggest in this part of Tibet. The 1996/1998 events are consistent with static stress transfer promoting failure. The Coulomb stress changes resulting from the 1996/1998 sequence also indicate that the westward dipping segment to the south-east has been advanced the most of the mapped faults to failure by stress increases.

Acknowledgments

HW is supported by the NSFC (41104016) and the State Key Laboratory of Earthquake Dynamics (LED2013B04). JRE and TJW are supported by the UK Natural Environmental Research Council (NERC) through the Earthquakes without Frontiers partnership (NE/J02001X/1) and the Centre for the Observation and Modelling of Earthquakes, Volcanoes and Tectonics (COMET). Envisat data are copy-righted by ESA and were provided under a category-1 project 13757. ASTER L3 data provided by NASA Land Processes Distributed Active Archive Center (LP DAAC), USGS/Earth Resources Observation and Science (EROS) Center, Sioux Falls, South Dakota. 2001. We thank the Editor-in-Chief Thorsten Becker, Romain Jolivet and an anonymous reviewer for their constructive comments that helped improve the manuscript. We used the JPL/Caltech ROI_PAC software to process InSAR data, and the Generic Mapping Tools [*Wessel and Smith*, 1998] to prepare the figures.

References

Abers, G. A. (2009), Slip on shallow-dipping normal faults, *Geology*, *37*(8), 767–768.

Aktug, B. et al. (2009), Deformation of western Turkey from a combination of permanent and campaign GPS data: Limits to block-like behavior, *J. Geophys. Res.*, *114*, B10404, doi:10.1029/2008JB006000.

Anderson, E. M. (1942), *The Dynamics of Faulting and Dyke Formation With Application to Britain*, Oliver and Boyd, Edinburgh.

Anderson, H., and J. Jackson (1987), Active tectonics of the Adriatic region, *Geophys. J. Int.*, *91*(3), 937–983.

Armijo, R., P. Tapponnier, J. L. Mercier, and T.-L. Han (1986), Quaternary extension in southern Tibet: Field observations and tectonic implications, *J. Geophys. Res.*, *91*(B14), 13,803–13,872.

Axen, G. J. (2004), Mechanics of low-angle normal faults, in *Rheology and Deformation in the Lithosphere at Continental Margins*, edited by G. Karner et al., pp. 46–91, Columbia Univ. Press, N. Y.

Axen, G. J. (2007), Research focus: Significance of large-displacement, low-angle normal faults, *Geology*, *35*(3), 287–288.

Biggs, J., E. Bergmann, B. Emmerson, G. J. Funning, J. Jackson, B. Parsons and T. J. Wright (2006), Fault identification for buried strike-slip earthquakes using InSAR: The 1994 and 2004 Al Hoceima, Morocco earthquakes, *Geophys. J. Int.*, *166*, 1347–1362.

Buck, W. (2007), Dynamic processes in extensional and compressional settings: The dynamics of continental breakup and extension, in *Treatise on Geophysics*, edited by G. Schubert, pp. 335–376, Elsevier, Amsterdam.

Bürgmann, R., P. A. Rosen, and E. J. Fielding (2000), Synthetic aperture radar interferometry to measure Earth's surface topography and its deformation, *Annu. Rev. Earth Planet. Sci.*, *28*, 169–209.

Byerlee, J. D. (1978), Friction of rocks, *Pure Appl. Geophys.*, *116*, 616–626.

Çemen, I. (2010), Extensional tectonics in the basin and range, the Aegean, and western Anatolia: Introduction, *Tectonophysics*, *488*(14), 1–6.

Cervelli, P., M. H. Murray, P. Segall, Y. Aoki, and T. Kato (2001), Estimating source parameters from deformation data, with an application to the March 1997 earthquake swarm off the Izu Peninsula, Japan, *J. Geophys. Res.*, *106*(B6), 11,217–11,237, doi:10.1029/2000JB900399.

Cogan, M. J., K. D. Nelson, W. S. F. Kidd, and C. Wu (1998), Shallow structure of the Yadong-Gulu rift, southern Tibet, from refraction analysis of Project INDEPTH common midpoint data, *Tectonics*, *17*(1), 46–61.

Collettini, C. (2011), The mechanical paradox of low-angle normal faults: Current understanding and open questions, *Tectonophysics*, *510*, 253–268.

Collettini, C. and R. H. Sibson (2001), Normal faults, normal friction?, *Geology*, *29*, 927–930.

Dawers, N. H., M. H. Anders, and C. H. Scholz (1993), Growth of normal faults: Displacement-length scaling, *Geology*, *21*, 1107–1110.

Eaton, G. P. (1982), The Basin and Range Province: Origin and tectonic significance, *Annu. Rev. Earth Planet. Sci.*, *10*(1), 409–440.

Ekström, G., M. Nettles, and A. Dziewónski (2012), The global CMT project 2004–2010: Centroid-moment tensors for 13,017 earthquakes, *Phys. Earth Planet. Inter.*, *200–201*, 1–9.

Elliott, J. R. (2009), Strain accumulation & release on the Tibetan Plateau measured using InSAR, Ph.D. thesis, Univ. of Oxford., Oxford, U. K.

Elliott, J. R., J. Biggs, B. Parsons, and T. J. Wright (2008), InSAR slip rate determination on the Altyn Tagh Fault, northern Tibet, in the presence of topographically correlated atmospheric delays, *Geophys. Res. Lett.*, *35*, L12309, doi:10.1029/2008GL033659.

Elliott, J. R., R. J. Walters, P. C. England, J. A. Jackson, Z. Li and B. Parsons (2010), Extension on the Tibetan plateau: Recent normal faulting measured by InSAR and body wave seismology, *Geophys. J. Int.*, *183*(2), 503–535.

Engdahl, E. R., R. van der Hilst, and R. Buland (1998), Global teleseismic earthquake relocation with improved travel times and procedures for depth determination, *Bull. Seismol. Soc. Am.*, *88*, 722–743.

England, P. C., and G. A. Houseman (1989), Extension during continental convergence, with application to the Tibetan Plateau, *J. Geophys. Res.*, *94*(B12), 17,561–17,579, doi:10.1029/JB094iB12p17561.

Farr, T. G., et al. (2007), The shuttle radar topography mission, *Rev. Geophys.*, *45*, RG2004, doi:10.1029/2005RG000183.

Feigl, K. L., and E. Dupré (1999), RNGCHN: A program to calculate displacement components from dislocations in an elastic half-space with applications for modeling geodetic measurements of crustal deformation, *Comput. Geosci*, *25*(6), 695–704.

Floyd, M. A., et al. (2010), A new velocity field for Greece: Implications for the kinematics and dynamics of the Aegean, *J. Geophys. Res.*, *115*, B10403, doi:10.1029/2009JB007040.

Funning, G. J., B. Parsons, T. J. Wright, J. A. Jackson and E. J. Fielding (2005), Surface displacements and source parameters of the 2003 Bam (Iran) earthquake from Envisat advanced synthetic aperture radar imagery, *J. Geophys. Res.*, *110*, B09406, doi:10.1029/2004JB003338.
Goldstein, R. M., and C. L. Werner (1998), Radar interferogram filtering for geophysical applications, *Geophys. Res. Lett.*, *25*(21), 4035–4038.
Goldstein, R. M., H. A. Zebker, and C. L. Werner (1988), Satellite radar interferometry: Two-dimensional phase unwrapping, *Radio Sci.*, *23*(4), 713–720.
Hammond, W. C., G. Blewitt, and C. Kreemer (2014), Steady contemporary deformation of the central Basin and Range Province, western United States, *J. Geophys. Res.*, doi:10.1002/2014JB011145, in press.
He, J., and G. Peltzer (2010), Poroelastic triggering in the 9-22 January 2008 Nima-Gaize (Tibet) earthquake sequence, *Geology*, *38*(10), 907–910.
Jackson, J. (1994), Active tectonics of the Aegean region, *Annu. Rev. Earth Planet. Sci.*, *22*(1), 239–271.
Jackson, J. and N. White (1989), Normal faulting in the upper continental crust: Observations from regions of active extension, *J. Struct. Geol.*, *11*, 15–36.
Jackson, J. A. (1987), Active normal faulting and crustal extension, *Geol. Soc. London Spec. Publ.*, *28*, 3–17.
Jónsson, S., H. Zebker, P. Segall, and F. Amelung (2002), Fault slip distribution of the 1999 M_w 7.1 Hector Mine, California, earthquake, estimated from satellite radar and GPS measurements, *Bull. Seismol. Soc. Am.*, *92*(4), 1377–1389.
Kali, E. (2010), De la déformation long-terme à court-terme sur les failles normales du Sud-Tibet: Approche géochronologique multi-méthodes (10Be,26Al,(U-Th)/He,^{40}Ar/^{39}Ar,U/Pb), PhD thesis, Univ. de Strasbourg., Strasbourg, France.
Kapp, P., and J. H. Guynn (2004), Indian punch rifts Tibet, *Geology*, *32*, 993–996.
Kapp, P., M. Taylor, D. Stockli, and L. Ding (2008), Development of active low-angle normal fault systems during orogenic collapse: Insight from Tibet, *Geology*, *36*(1), 7–10.
Langin, W. R., L. D. Brown, and E. A. Sandvol (2003), Seismicity of central Tibet from Project INDEPTH III seismic recordings, *Bull. Seismol. Soc. Am.*, *93*, 2146–2159.
Lin, J., and R. S. Stein (2004), Stress triggering in thrust and subduction earthquakes and stress interaction between the southern san andreas and nearby thrust and strike-slip faults, *J. Geophys. Res.*, *109*, B02303, doi:10.1029/2003JB002607.
Lohman, R. B., and M. Simons (2005), Some thoughts on the use of InSAR data to constrain models of surface deformation, *Geochem. Geophys. Geosyst.*, *6*, Q01007, doi:10.1029/2004GC000841.
Massonnet, D., and K. L. Feigl (1998), Radar interferometry and its application to changes in the Earth's surface, *Rev. Geophys.*, *36*(4), 441–500.
McCaffrey, R., and J. Nabelek (1998), Role of oblique convergence in the active deformation of the Himalayas and southern Tibet plateau, *Geology*, *26*, 691–694.
Middleton, T. A., and A. Copley (2014), Constraining fault friction by re-examining earthquake nodal plane dips, *Geophys. J. Int.*, *196*(2), 671–680.
Molnar, P., and H. Lyon-Caen (1989), Fault plane solutions of earthquakes and active tectonics of the Tibetan Plateau and its margins, *Geophys. J. Int.*, *99*(1), 123–154.
Molnar, P., and P. Tapponnier (1978), Active tectonics of Tibet, *J. Geophys. Res.*, *83*(B11), 5361–5375.
Monigle, P. W., J. Nabelek, J. Braunmiller, and N. S. Carpenter (2012), Evidence for low-angle normal faulting in the Pumqu-Xianza Rift, Tibet, *Geophys. J. Int.*, *190*(3), 1335–1340.
Nocquet, J.-M. (2012), Present-day kinematics of the Mediterranean: A comprehensive overview of GPS results, *Tectonophysics*, *579*, 220–242.
Okada, Y. (1985), Surface deformation due to shear and tensile faults in a half-space, *Bull. Seismol. Soc. Am.*, *75*(4), 1135–1154.
Parsons, B., T. Wright, P. Rowe, J. Andrews, J. Jackson, R. Walker, M. Khatib, M. Talebian, E. Bergman and E. R. Engdahl (2006), The 1994 Sefidabeh (eastern Iran) earthquake revisited: New evidence from satellite radar interferometry and carbonate dating about the growth of an active fold above a blind thrust fault, *Geophys. J. Int.*, *164*, 202–217.
Rosen, P. A., S. Hensley, G. Peltzer, and M. Simons (2004), Updated repeat orbit interferometry package released, *Eos Trans. AGU*, *85*(5), 47.
Ryder, I., R. Burgmann, and E. Fielding (2012), Static stress interactions in extensional earthquake sequences: An example from the South Lunggar Rift, Tibet, *J. Geophys. Res.*, *117*, B09405, doi:10.1029/2012JB009365.
Scharroo, R., and P. Visser (1998), Precise orbit determination and gravity field improvement for the ERS satellite, *J. Geophys. Res.*, *103*(C4), 8113–8127.
Scholz, C. H., and P. A. Cowie (1990), Determination of total strain from faulting using slip measurements, *Nature*, *346*, 837–839.
Searle, M. P., J. R. Elliott, R. J. Phillips, and S.-L. Chung (2011), Crustal-lithospheric structure and continental extrusion of Tibet, *J. Geod.*, *168*, 633–672.
Sibson, R. H., and G. Xie (1998), Dip range for intracontinental reverse fault ruptures: Truth not stranger than friction?, *Bull. Seismol. Soc. Am.*, *88*(4), 1014–1022.
Simons, M., Y. Fialko, and L. Rivera (2002), Coseismic deformation from the 1999 M_w 7.1 Hector Mine, California, earthquake as inferred from InSAR and GPS observations, *Bull. Seismol. Soc. Am.*, *92*(4), 1390–1402.
Sloan, R. A., J. A. Jackson, D. McKenzie, and K. Priestley (2011), Earthquake depth distributions in central Asia, and their relations with lithosphere thickness, shortening and extension, *Geophys. J. Int.*, *185*(1), 1–29.
Steck, L. K., W. S. Phillips, K. Mackey, M. L. Begnaud, R. J. Stead, and C. A. Rowe (2009), Seismic tomography of crustal P and S across Eurasia, *Geophys. J. Int.*, *177*(1), 81–92.
Taylor, M., and A. Yin (2009), Active structures of the Himalayan-Tibetan orogen and their relationships to earthquake distribution, contemporary strain field, and Cenozoic volcanism, *Geosphere*, *5*(3), 199–214.
Taymaz, T., J. Jackson, and R. Westaway (1990), Earthquake mechanisms in the Hellenic trench near Crete, *Geophys. J. Int.*, *102*, 424–443.
Taymaz, T., J. Jackson, and D. McKenzie (1991), Active tectonics of the north and central Aegean Sea, *Geophys. J. Int.*, *106*, 433–490.
Thatcher, W., and D. P. Hill (1991), Fault orientations in extensional and conjugate strike-slip environments and their implications, *Geology*, *19*, 1116–1120.
Wang, H., and T. J. Wright (2012), Satellite geodetic imaging reveals internal deformation of western Tibet, *Geophys. Res. Lett.*, *39*, L07303, doi:10.1029/2012GL051222.
Wells, D. L., and K. J. Coppersmith (1994), New empirical relationships among magnitude, rupture length, rupture width, rupture area and surface displacement, *Bull. Seismol. Soc. Am.*, *84*(4), 974–1002.
Wernicke, B. (1995), Low-angle normal faults and seismicity: A review, *J. Geophys. Res.*, *100*(B10), 20,159–20,174.
Wernicke, B., G. J. Axen and J. K. Snow (1988), Basin and Range extensional tectonics at the latitude of Las Vegas, Nevada, *Geol. Soc. Am. Bull.*, *100*, 1738–1757.

Wessel, P., and W. H. F. Smith (1998), New, improved version of Generic Mapping Tools released, *Eos Trans. AGU*, *79*(47), 579.
Weston, J., A. M. Ferreira, and G. J. Funning (2012), Systematic comparisons of earthquake source models determined using InSAR and seismic data, *Tectonophysics*, *532–535*, 61–81.
Wright, T. J., Z. Lu, and C. Wicks (2003), Source model for the M_w 6.7, 23 October 2002, Nenana Mountain earthquake (Alaska) from InSAR, *Geophys. Res. Lett.*, *30*(18), 1974, doi:10.1029/2003GL018014.
Wright, T. J., Z. Lu, and C. Wicks (2004), Constraining the slip distribution and fault geometry of the M_w 7.9 3 November 2002, Denali Fault earthquake with interferometric synthetic aperture radar and global positioning system data, *Bull. Seismol. Soc. Am.*, *94*(6B), S175–S189.
Wright, T. J., J. R. Elliott, H. Wang, and I. Ryder (2013), Earthquake cycle deformation and the moho: Implications for the rheology of continental lithosphere, *Tectonophysics*, *609*, 504–523.
Yin, A. (2000), Mode of Cenozoic east-west extension in Tibet suggesting a common origin of rifts in Asia during the Indo-Asian collision, *J. Geophys. Res.*, *105*(B9), 21,745–21,760.
Ziv, A., M.-P. Doin, and R. Grandin (2013), What can be learned from underdetermined geodetic slip inversions: The Parkfield GPS network example, *Geophys. J. Int.*, *194*, 1900–1908.
Zwick, P., R. McCaffrey, and G. Abers (1994), MT5 program, *IASPEI Software Libr.*, *4*.